Wettability and brazing of (MoNbTaVW)C High-Entropy Carbide by Ni and NiTa

Journal of Materials Research and Technology 39 (2025) 1599–1611

Contents lists available at ScienceDirect

Journal of Materials Research and Technology

journal homepage: www.elsevier.com/locate/jmrt

# Wettability and brazing of (MoNbTaVW)C high-entropy carbide by Ni and NiTa

Naser Hosseini [a], Fabrizio Valenza [b], Zdeněk Chlup [c], Sofia Gambaro [b], Filip Šiška [c], Carla Malinverni [d], Jie Xu [e], Valentina Casalegno [d], Alexandra Kovalčíková [f], Monika Tatarková [a], Milena Salvo [d], Xiaobing Zhou [e], Ivo Dlouhý [c], Peter Tatarko [a,*]

[a] Institute of Inorganic Chemistry, Slovak Academy of Sciences, Dúbravská Cesta 9, 845 36, Bratislava, Slovakia
[b] Institute of Condensed Matter Chemistry and Technologies for Energy–ICMATE, National Research Council –CNR, Via De Marini 6, 16149, Genoa, Italy
[c] Institute of Physics of Materials, Czech Academy of Sciences, Žižkova 22, 616 00, Brno, Czech Republic
[d] Department of Applied Science and Technology, Politecnico di Torino, Corso Duca Degli Abruzzi 24, 10129, Torino, Italy
[e] Zhejiang Key Laboratory of Data-Driven High-Safety Energy Materials and Applications, Ningbo Key Laboratory of Special Energy Materials and Chemistry, Ningbo Institute of Materials Technology and Engineering, Chinese Academy of Sciences, Ningbo, 315201, China
[f] Institute of Materials Research, Slovak Academy of Sciences, Watsonova 47, 04001, Košice, Slovakia

ARTICLE INFO

*Keywords:*
High entropy carbides
Wetting
Brazing
Nickel
NiTa alloy

ABSTRACT

This study aimed to design and validate a suitable brazing filler for the joining of (MoNbTaVW)C High-Entropy Carbides (HECs). CALPHAD calculations were used to analyse phase equilibria of ternary C–Ni-M (M: Mo, Ta, W) systems at 1480 °C and to select a suitable alloy composition for brazing. Wettability and high-temperature interactions with the HEC substrates were investigated using the sessile drop technique. While pure Ni provided a good wetting (≤15°) but an excessive dissolution, the $Ni_{83}Ta_{17}$ alloy exhibited a comparable wetting with a significantly reduced dissolution due to the formation of interfacial $TaC_x$-rich phases. Consequently, the NiTa alloy was employed as a filler to braze HEC ceramics using a pressure-less field-assisted sintering technique (FAST) furnace at 1480 °C, resulting in a crack-free, homogeneous joint. The interfacial $TaC_x$-rich phase exhibited a high nano-hardness (~24 GPa) and indentation elastic modulus (~311 GPa). Single-lap offset shear tests confirmed a very high strength of the joints (~220 MPa), demonstrating the viability of the NiTa alloy for joining HEC.

## 1. Introduction

High-entropy carbides (HEC) have garnered significant interest as potential materials for engineering applications (such as drill bits and cutting tools) and extreme environments (such as turbine engines, next-generation nuclear reactors, and hypersonic vehicles). This interest is due to their high hardness, excellent thermal stability, and good irradiation, oxidation, corrosion, and wear resistance [1–5]. The concept of high-entropy materials, which is single-phase solid solutions of inorganic compounds consisting of four or more cations stabilised by a high configurational entropy, offers excellent opportunities for the development of novel carbides with a wide range of properties and applications [6].

The first synthesis of high-entropy carbide in 2018 b y Castle et al. marked a major step forward in the development of carbide ceramics [7]. Since then, HECs have been developed and characterised in various compositions, such as (HfNbTaTiZr) C [3], (TiZrNbTaW) C [8], (TaNbTiVW) C [9], and (MoNbTaVW) C [10]. HECs have shown improved hardness and fracture toughness compared to their conventional binary counterparts (such as NbC, TaC, HfC, and ZrC) [11]. However, the intrinsic brittleness of ceramics presents a significant challenge in fabricating large and complex-shaped bulk HEC ceramics via sintering and machining. Consequently, the further expansion of the potential application of HEC requires the development of reliable, user-friendly, and cost-effective joining techniques [12–14].

Various techniques, such as brazing [15], solid-state diffusion bonding with metallic interlayers [16], glass-ceramic joining [17], and direct bonding [18], have been used to join ceramic materials. Among these techniques, brazing has attracted significant attention due to its versatility, efficiency, and ability to join dissimilar materials with high

* Corresponding author.
*E-mail address:* peter.tatarko@savba.sk (P. Tatarko).

https://doi.org/10.1016/j.jmrt.2025.09.182
Received 25 March 2025; Received in revised form 17 September 2025; Accepted 18 September 2025
Available online 19 September 2025

strength and good integrity [19,20]. Brazing relies on molten interlayers that distribute along the adjoining surfaces, assuring adhesion. Therefore, the composition of a brazing filler, its wetting, and the consequent molten metal/ceramic interfacial interactions, play important roles in the joining of ceramics [21,22].

During the last few years, the interfacial interactions of HEC ceramics and metals have been investigated to advance the development of an appropriate joining approach for this emerging class of ceramics [23]. Moreover, the interaction of HEC ceramics with Ni, Co, and Fe metals is of significant interest in the field of ceramic-metal composites (cermets) for cutting tools and wear-resistant applications [24,25]. Mu et al. joined (HfTaZrNbTi) C to itself with a Ni foil using a solid-state diffusion bonding in a hot press at 1200 °C with a maximum pressure of 10 MPa and a dwell time of 60 min [26]. They concluded that the formation of the $Ti_2Ni$ compound at the interface was the reason for the relatively high shear strength of the joints (151 MPa). Sun et al. investigated the interfacial interactions and joining of (HfTaZrNbTi) C with TiNi–20Nb eutectic alloy using the active brazing technique at temperatures ranging from 1180 to 1220 °C, with a dwell time of 10 min in a hot press [27]. They reported that the thickness and composition of the reaction layer significantly affected the strength of the joints. Specifically, when the brazing temperature increased up to 1200 °C, the thickness of the (Ti,Nb) C reaction layer decreased, while the brittle $(Ti,Nb)_2Ni$ layer thickened, leading to a reduction in joint strength to 171 MPa. Wang et al. brazed (TiZrNbTaCr) C to Nb metal using a $BNi_2$ commercial filler (Ni–7Cr-4.5Si–3B–3Fe (at.%)) at 1170 °C with a dwell time of 10 min in a vacuum furnace [28]. The bonding process occurred through the diffusion of Nb, resulting in the formation of a diffusion zone with Nb and a reaction layer of NbC. At room temperature, the HEC-Nb joints exhibited a maximum shear strength of 136 MPa, while the shear strength slightly decreased to 119 MPa at 800 °C. Vedel et al. studied the wettability and the interfacial reactivity of Fe, Co, Ni on (TiZrHfNbTa) C [29]. The dissolution of ceramics and metal penetration into the substrate led to a good wetting with a final contact angle of 20°, 30°, and 22°, for Fe, Co, and Ni, respectively. They concluded that (Nb, Ta)C-solid solution carbide, ZrC-based solid solution carbide, and $Me_5$(Ti,Zr,Hf) intermetallic were formed at the interface.

More recently, the high-temperature interactions of HEC in contact with high entropy alloys have been investigated. The wettability and interfacial behaviour of FeCoCrNiTi high-entropy alloy on (HfZrTiTaNb) C substrate were studied by Mu et al. [30,31]. The bonding mechanism was attributed to the formation of a metallic Ti-rich layer, depleted in Zr and Hf relative to the original HEC composition. The formation of this interfacial carbide layer led to a superior shear strength of 292 MPa for the joints brazed at 1430 °C. Recently, Niu et al. employed a Ti–Zr–Ni–Cu alloy for the joining of (VNbTaMoW) C at a temperature of 980 °C with a dwell time of 10 min in a vacuum furnace [32]. It was shown that the reaction between zirconium (as an active element) from the brazing alloy and carbon from the ceramic substrate led to the formation of a continuous (Zr,Ti,Nb) C layer, which significantly contributed to a relatively high shear strength (193 MPa).

Therefore, the interaction between metals and ceramics, particularly the formation of carbide phases at their interface, is critical in governing the interfacial bonding and mechanical integrity of metal-ceramic systems [33]. The selection of brazing alloys for joining of HECs requires careful optimisation based on multiple criteria, including chemical compatibility, wettability, melting temperature, and thermal expansion. Active elements, such as Ti (in Ag–Cu–Ti) [34] and Ni (in Ni-based systems) [35,36], promote wetting and adhesion by the formation of reactive interfacial compounds with the ceramic surface. In contrast, non-active elements, such as Cu, do not chemically react with the ceramic part, but can still serve as reference systems to evaluate fundamental wetting behaviour and diffusion at the interface [34]. Regardless of whether active or inert elements are used, their incorporation into a brazing alloy must be systematically tailored to ensure sufficient wetting, mechanical compatibility, and thermal stability with HECs during the joining process. Despite the significance of metal/-ceramic systems in the brazing of HEC ceramics and HEC ceramic-metal composites, the current state of the art lacks a systematic investigation into the wetting behaviour, interfacial reactions, and high-temperature stability of these systems. Addressing this limitation is crucial for enhancing our understanding of interfacial phenomena and enabling the development of more reliable and high-performance metal-ceramic systems for advanced engineering applications.

This study investigated the wetting behaviour and interfacial interactions between (MoNbTaVW) C high-entropy carbide and molten pure Ni and a Ni-17.2 at.% Ta alloy (hereafter: NiTa). Ni was selected as the base element due to its high melting point (1455 °C), stability, relatively good wettability with ceramics, mechanical strength, and availability [37,38]. CALPHAD (Calculation of Phase Diagrams) calculations were used to analyse relevant phase diagrams. The wetting behaviour of pure Ni and NiTa on the HEC surface was experimentally evaluated. Based on these analyses, NiTa was selected as the filler material for brazing. This work represents the first systematic study of the wetting behaviour and interfacial reactions of both pure Ni and the NiTa alloy with HEC ceramics, and demonstrates the successful joining of these HEC ceramics using NiTa as a brazing filler.

## 2. Experimental procedure

### 2.1. Substrate materials

The (MoNbTaVW) C HEC substrates were prepared using a field-assisted sintering technology (FAST) machine (DSP 507, Dr. Fritsch), following the sintering process reported in our previous work [10]. Briefly, $Mo_2C$ (99.5 %, ~ 325 mesh, Alfa Aesar), NbC (99 %, <10 μm, Alfa Aesar), TaC (99.5 %, ~ 325 mesh, Alfa Aesar), VC (99.0 %, ~325 mesh, Alfa Aesar), WC (99.5 %, <1 μm, Alfa Aesar) and an appropriate amount of carbon black (Vulcan PF, CS Cabot, ~ 325 mesh) were used as the starting materials. The carbon black powder was used to achieve the monocarbide composition of MoC. The individual powders corresponding to an equimolar composition were weighed in a glove box in an Ar atmosphere. Then, the powder mixture was milled using a planetary ball mill (PM100, Retsch) in a WC jar with WC balls (⌀ 10 mm) for 4 h at a speed of 250 rpm. The process was followed by drying the powder mixture in a vacuum evaporator (1 h) and a vacuum oven (24 h). After filling the dried powder mixtures in a graphite die with a 20 mm diameter, the sintering was performed by FAST at 1600 °C for 15 min under the pressure of 70 MPa in Ar atmosphere. Finally, the HEC discs were cut to a rectangular shape ($12 \times 12 \times 3$ $mm^3$), and the surfaces to be joined were polished up to the final polish using 1 μm diamond suspension. Before the wetting and brazing process, the HEC substrates were ultrasonically cleaned in isopropanol for 3 min, and dried in air.

### 2.2. Ni and NiTa alloy preparation

The mono-element metals, such as Ni (a purity of 99.99 %, wire, Goodfellow, Hungtingdon, UK), and Ta (a purity of 99 %, sheet, Goodfellow, Hungtingdon, UK), were used as the raw materials for the preparation of $Ni_{82.8}Ta_{17.2}$ eutectic alloy (hereafter referred to as NiTa). An appropriate amount of each metal was cut, weighed, and arc melted (Compact Arc Melter MAM-1, Edmund Buhler) in an Ar atmosphere. Pure Ni was melted only once to make it in a droplet shape, while the NiTa alloy was melted at least five times to homogenise the composition (Fig. 1a). The aforementioned arc melting setup was conducted on a water-cooled copper base plate. After each melting cycle, the alloy solidified directly on the copper surface, resulting in rapid cooling within a few seconds. This setup ensured consistent and reproducible solidification conditions for all samples. Pure Ni and NiTa alloy were used in the form of droplets, which were obtained by arc melting. To use NiTa alloy as the brazing filler, the drop-shaped alloy was crushed into particles smaller than 400 μm using a WC mortar and pestle.

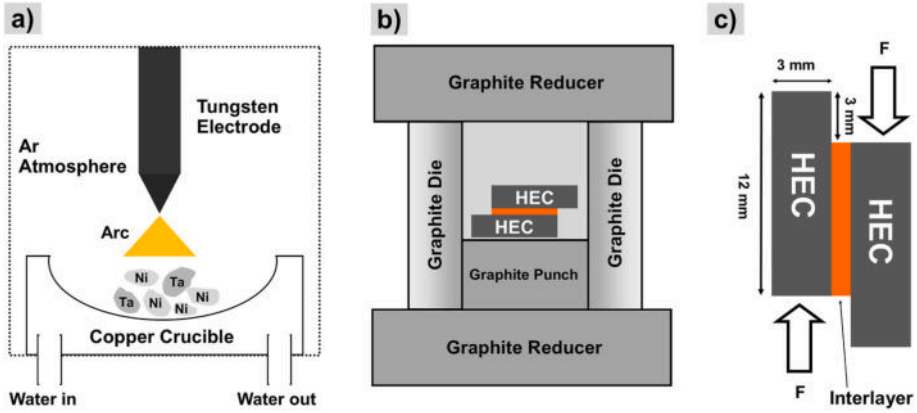


**Fig. 1.** Schematic illustration of a) arc melting technique for NiTa alloy preparation, b) die design for pressure-less brazing in a FAST machine, c) single lap offset shear test of brazed HEC ceramics.

### 2.3. Wetting experiments

The setup for wetting experiments was designed based on the sessile-drop technique [39]. The wetting experiments were performed at 1480 °C (25 °C above the melting point of Ni). While the NiTa alloy melts at a lower temperature (~1368 °C [40]) than pure Ni (1455 °C), 1480 °C was used for the wetting experiment of both materials to ensure comparability. A protective atmosphere (Ar/5 % $H_2$, static) was used, and Zr foils surrounding the samples acted as a getter to minimise oxygen contamination. The metal/HEC couples were rapidly introduced into the furnace hot zone (approximately 30 s) using an external push rod to minimise heating ramp times. During the experiment, the metal/HEC couple were continuously observed by a CCD camera and the contact angles were measured. Contact angles were continuously monitored via a CCD camera during the 5-min hold at 1480 °C. Subsequently, the samples were rapidly withdrawn from the hot zone (approximately 20 s) and cooled to room temperature within the same protective atmosphere.

### 2.4. Brazing procedure

The crushed NiTa alloy was placed between two HEC ceramics (12 × 12 × 3 $mm^3$) in a graphite die with a diameter of 20 mm. The HEC ceramics were joined along a 12 × 12 $mm^2$ surface with an offset, resulting in a consistent joined surface area of 9 × 12 $mm^2$ (Fig. 1c). The thickness of the interlayer was controlled by the amount of NiTa (2 × $10^{-3}$ g/$mm^2$), which was consistently maintained by using the same quantity each time. The brazing was performed at 1480 °C for 5 min in an Ar atmosphere using a FAST machine (DSP 507, Dr. Fritsch) without applying any pressure on the HEC/metal/HEC assembly. Fig. 1b presents a schematic diagram of the pressure-less die design for brazing in a FAST machine. The heating and cooling rates were kept constant at 100 °C/min and 15 °C/min, respectively.

### 2.5. Characterisation

The phase compositions and structures of the sintered HEC ceramics and the arc-melted NiTa alloy were analysed using X-ray diffraction (XRD; Panalytical Empyrean, Cu Kα radiation). Scanning electron microscopy (Lyra 3 XMU FEG, Tescan, or AURIGA Compact, Zeiss) coupled to EDS was used to characterise the microstructure and elemental composition of the sintered HEC ceramics, arc-melted NiTa alloy, as well as the cross-sections of the wetted and brazed ceramics. A transmission electron microscope (TEM, Talos™ F200x, Thermo Fisher Scientific, USA) equipped with an energy-dispersive X-ray spectrometry (EDS) detector was used to determine the microstructure and phase compositions of the joining interlayer. The specimens for the TEM observations were machined using a focused ion beam technique (FIB, Auriga, Carl Zeiss).

The linear thermal expansion measurement of (MoNbTaVW) C HEC ceramics was carried out using a NETZSCH DIL 402C thermal dilatometer under an argon atmosphere over the temperature range of 25–1300 °C. Both heating and cooling were performed at a rate of 3 °C/min. The ceramic sample size for measurement was 4 × 4 × 12 $mm^3$. The coefficient of thermal expansion (CTE) was determined based on the measured dimensional changes.

The nanoindentation technique was performed on a Zwick ZHN nanomechanical machine using a Vickers indenter. The force-controlled test with a maximal load of 250 mN (HV0.25) was used to measure the hardness and indentation elastic modulus of the joined area.

The mechanical strength of the brazed HEC ceramics was evaluated by a Single Lap Offset (SLO) shear test at room temperature using a universal testing machine (SINTEC D/10) with a crosshead speed of 0.5 mm/min and a 50 kN load cell (Fig. 1c). The employed method for testing was adapted from the ASTM D1002–05 standard. The maximum force was recorded, and the apparent shear strength was calculated by dividing the maximum force by the joining area. Further information on the SLO set-up is available in Ref. [41]. The results of SLO mechanical tests were expressed as the average value of five brazed samples.

## 3. Results and discussion

### 3.1. Thermodynamic evaluation by ternary phase diagrams

To predict and understand potential interactions between HEC substrate and liquid Ni-based alloys at the experimental temperature, a thermodynamic analysis using CALPHAD method was performed. Ideally, a complete analysis would involve seven elements (C, Mo, Nb, Ni, Ta, V, and W), but this is computationally demanding due to the complexity of the system and the need for accurate thermodynamic databases. The in-house thermodynamic database, named GHEA, was created at Genoa University and validated by some of the authors [42,43], encompasses key HEC elements, including C, Mo, Ta, and W. Therefore, to simplify this prediction and extract practical insights concerning the high-temperature reactivity, ternary C–Ni-M (M: Mo, Ta, W) systems were selected, and the related isothermal sections at 1480 °C calculated using this database and Thermo-Calc® software (Fig. 2). Unfortunately, the GHEA database still does not include Nb and V, and no data are available in literature or commercial databases. This prevents a fully comprehensive assessment of all HEC elements. However, due to the chemical similarities of Nb and V to Ta and their comparable binary interactions with C or Ni, similar reactivity trends are anticipated for these elements.

The isothermal sections of the phase diagrams revealed the presence

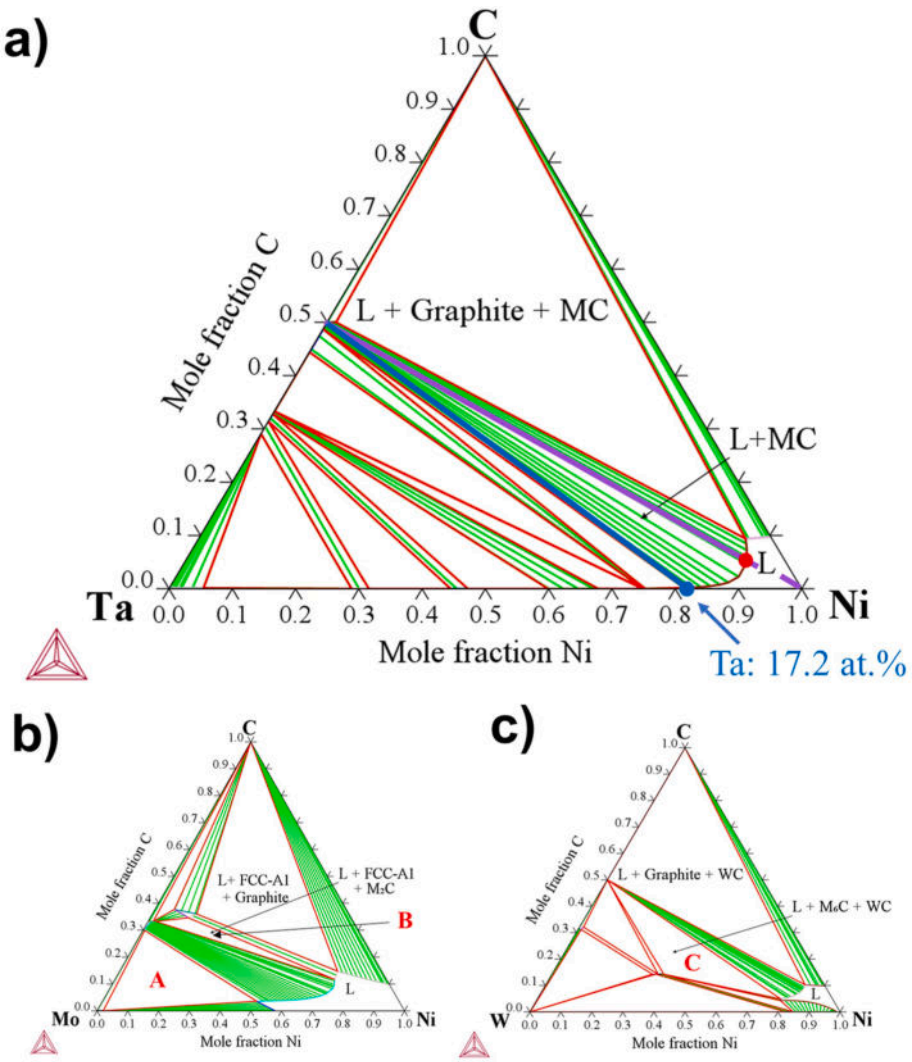


**Fig. 2.** Isothermal sections calculated at 1480 °C by the use of Thermo-Calc® software and GHEA database for: a) C–Ni–Ta, b) C–Ni–Mo, c) C–Ni–W systems.

of extensive liquid regions in Ni corners. This suggests that molten Ni can dissolve significant amounts of carbides, similar to the earlier observations on the liquid Ni in contact with SiC [44]. This dissolution process can be detrimental to the ceramics, as it continues until chemical equilibrium is reached, resulting in multiphase regions containing a saturated liquid, graphite, and carbide. A viable strategy to mitigate dissolution involves alloying pure Ni with elements from the ceramics themselves to pre-saturate the alloy, as seen in the systems, such as Ni–Si/SiC [44], Ni–B/$ZrB_2$ [45] and Ni–B/$HfB_2$ [35]. Therefore, considering the chemical composition of the present HEC ceramics, elements including Mo, V, W, Nb, and Ta are potential alloying elements.

The Ni–Mo–C and Ni–W–C systems (shown in Fig. 2b and c, respectively) show larger liquid regions, resulting in greater dissolution and the formation of ternary phases. In the Ni–Mo–C system, carbide dissolution persists across binary Ni–Mo compositions, resulting in distinct three-phase equilibrium regions, such as regions A and B, where excess liquid promotes both carbide dissolution and the formation of additional phases. Similarly, in the Ni–W–C system, a binary Ni–W alloy still dissolves carbide, leading to an equilibrium three-phase region (region C), characterised by the formation of a ternary phase ($M_6C$).

In contrast, Ni–Ta–C stands out as particularly promising. The isothermal section (Fig. 2a) reveals that Ni can dissolve TaC (purple line), with the liquid composition gradually shifting towards the red point. This ultimately results in a stable three-phase equilibrium involving a liquid, TaC, and graphite. Notably, the addition of Ta to Ni significantly mitigates the dissolution of TaC. As the liquidus line approaches the Ni–Ta binary system, the amount of TaC required for saturation decreases. In this equilibrium area at isothermal sections at 1480 °C, the liquid phase reaches saturation without any additional dissolution of TaC. As anticipated, according to their chemical similarities to Ta, similar trends are expected for Nb and V; nonetheless, Ta was chosen as an alloying element given the more appealing thermal properties of TaC.

The formation of a ternary phase resulting from the ceramic substrate dissolution is undesirable in brazing filler alloy design. This analysis highlights the complexity of phase equilibria in ternary systems. The Ni–Ta–C system emerges as a promising candidate for further study, particularly due to the limited substrate dissolution, accompanied by the formation of carbide phases. The hypereutectic composition of the Ni–Ta binary system (17.2 at.% Ta in Ni [46]), indicated by the blue point in Fig. 2a, is a potential NiTa brazing filler candidate. This composition offers a promising starting point for experimental investigation, avoiding extensive and costly preliminary studies.

### 3.2. *Characterisation of HEC substrate and NiTa alloy*

Fig. 3a presents the XRD patterns of the sintered HEC ceramics and the arc-melted NiTa alloy, while Fig. 3b and c shows the SEM microstructures of both materials, respectively. Nearly fully dense (relative density of 98 %), single-phase (MoNbTaVW) C HEC ceramics with the

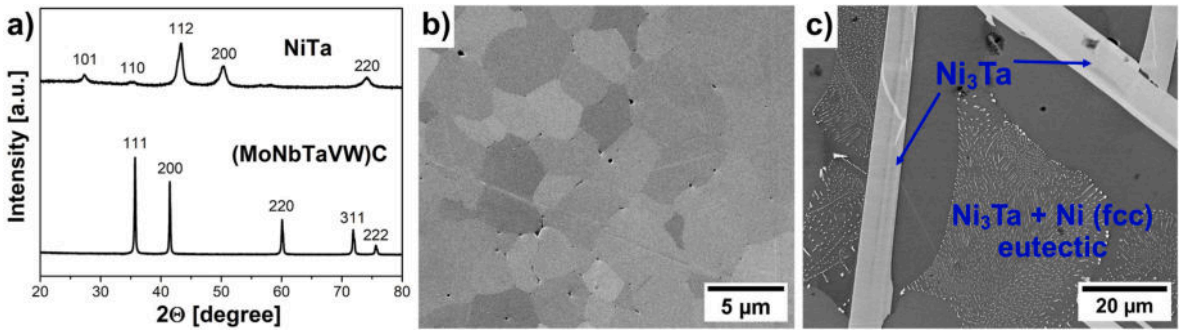


**Fig. 3.** a) XRD patterns of the as-prepared HEC ceramics and NiTa alloy; SEM microstructure of the as-prepared b) HEC ceramics and c) NiTa alloy.

rock-salt crystal structure were successfully prepared. The different colours observed in Fig. 3b arise from variations in the crystallographic orientations of individual grains, which affect the image contrast signal in the SEM image [3,10]. The details about the characterisation of the HEC substrate can be found in our previous work [10]. The XRD (Fig. 3a) and SEM (Fig. 3c) analyses confirmed that the eutectic reaction of Liquid → fcc (Ni) + $Ni_3Ta$ occurred in the arc-melted Ni–Ta alloy. The $Ni_3Ta$ phases crystallised in a plate-like morphology (bright phase in Fig. 3c), and eutectic phases formed between $Ni_3Ta$ and Ni (fcc) matrix. A similar phase evolution for the Ni–Ta system was observed by Chenyang Zhou et al. [47].

### 3.3. Wetting of HEC by molten pure Ni

Fig. 4 illustrates the evolution of the contact angle with time, along with the photographs showing the sessile drops at various time intervals for pure Ni on the HEC surface at 1480 °C. The molten Ni drop began spreading upon melting at 1480 °C, reaching a contact angle of ≤18° within approximately 75 s (Stage I). Subsequently, over the next 225 s, the molten metal continued to spread and stabilised at a relatively constant contact angle of ≤15° (Stage II).

Fig. 5 presents the SEM microstructure of the cross-sectioned Ni/HEC couple at different magnifications (Fig. 5a–c), and the top surface of solidified Ni (Fig. 5d and e). The SEM analysis revealed the presence of significant cracks, as shown in Fig. 5a. These were likely formed due to differences in the CTE between HEC and pure Ni. The measured CTE value for (MoNbTaVW) C HEC in this work was ~$7.65 \times 10^{-6}\,K^{-1}$, while for pure Ni, the reported values were $15.4 - 19 \times 10^{-6}\,K^{-1}$ [48,49]. The CTE mismatch caused the formation of residual stresses in the samples, which led to the formation of cracks upon rapid cooling, as the HEC/Ni couple was removed from the furnace within 20 s. Such crack formation in wetting experiments has also been reported in previous studies involving metal/ceramic systems [29,30,35]. A concave shaped interface was observed in the central region, clearly indicating a substantial dissolution of the HEC substrate by the liquid metal. Upon saturation of molten Ni with elements from HEC, the drop spread further across the substrate without additional dissolution. The resulting sigmoidal interface profile (shown by dashed rectangles in Fig. 5a) highlights the interplay between dissolution and spreading of the saturated alloy, a phenomenon generally recognised as dissolutive wetting [50].

A significant HEC dissolution into the molten Ni was also confirmed by the SEM/EDS analysis of the top surface of the solidified alloy, as considerable amounts of elements from the ceramics were detected (Table 1 for the selected points in Fig. 5d and e). This indicated that elements from the ceramics dissolved into the molten Ni and migrated away from the interface towards the top surface of the liquid. Upon solidification, these elements formed distinct phases on the top surface of Ni. Notably, Ta and Nb-rich phases originating from the HEC ceramics segregated into star-shaped structures within the solidified molten Ni (labelled D). The precise mechanism for the formation of these unique structures is not yet fully understood and requires further investigation.

A reaction layer with a thickness of ~70 μm was observed along the interface (Fig. 5a). A higher magnification of the reaction layer is shown in Fig. 5b, where the dark regions (labelled A) correspond to Ni-rich solid solution, while the bright areas (labelled B) represent HEC grains. The presence of a small amount of the elements originating from the HEC substrate in Ni (A in Table 1) suggested that the HEC grains dissolved into molten Ni. On the contrary, the presence of Ni in HEC grains (B in Table 1) revealed that Ni diffused into the ceramic grains. The diffusion of Ni into the lattice of HEC was also reported by Mu et al. [26].

The formation of carbide-rich phases at the Ni/HEC interface was

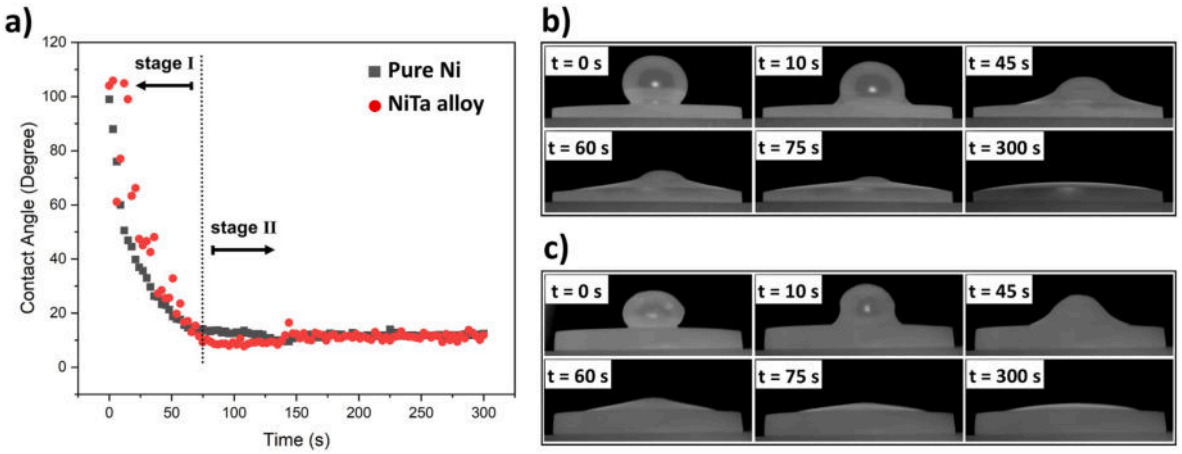


**Fig. 4.** a) Evolution of the contact angle with time for molten pure Ni and NiTa alloy on the HEC substrate at 1480 °C; photographs of molten sessile drops of b) pure Ni, and c) NiTa alloy on the HEC substrate at 1480 °C at different time intervals.

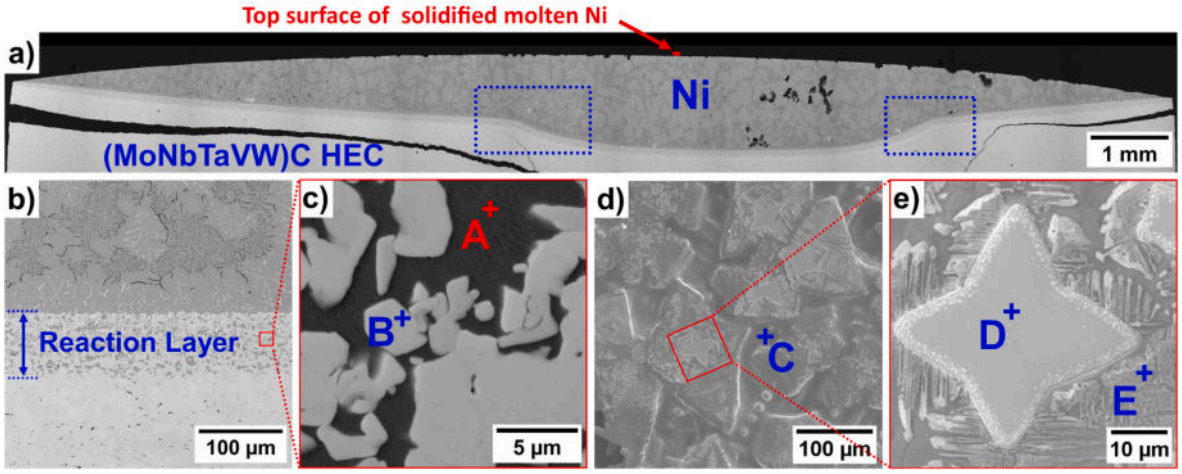


**Fig. 5.** a-c) SEM microstructure of the cross-section of the HEC/Ni couple at different magnifications; d and e) SEM images of the top surface of solidified Ni after the wetting experiment at 1480 °C.

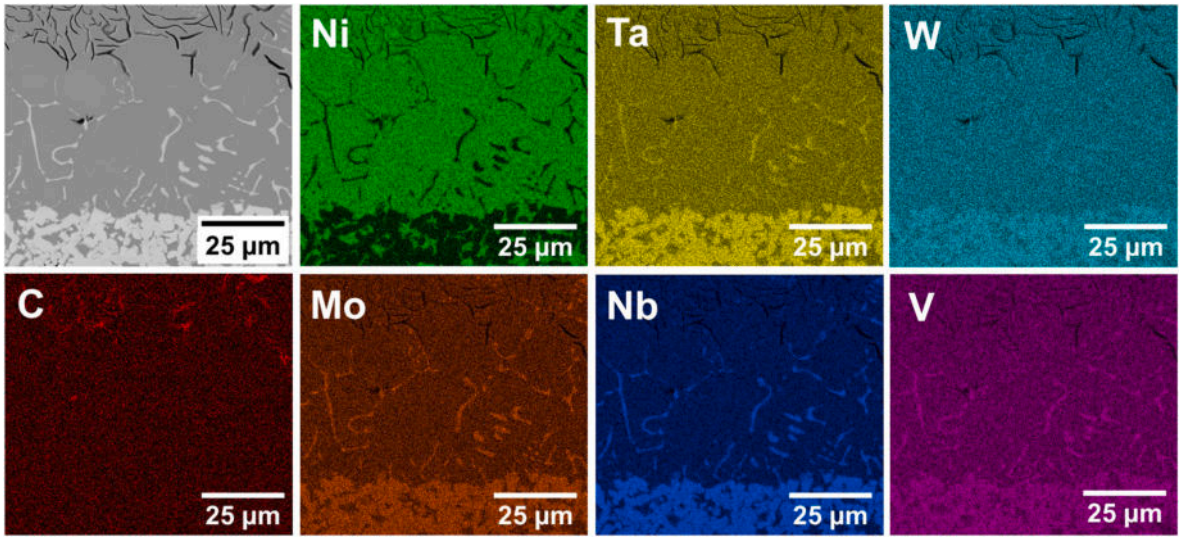


**Fig. 6.** SEM microstructure of the cross-section of HEC/Ni couple after the wetting experiment at 1480 °C and the corresponding EDS mapping.

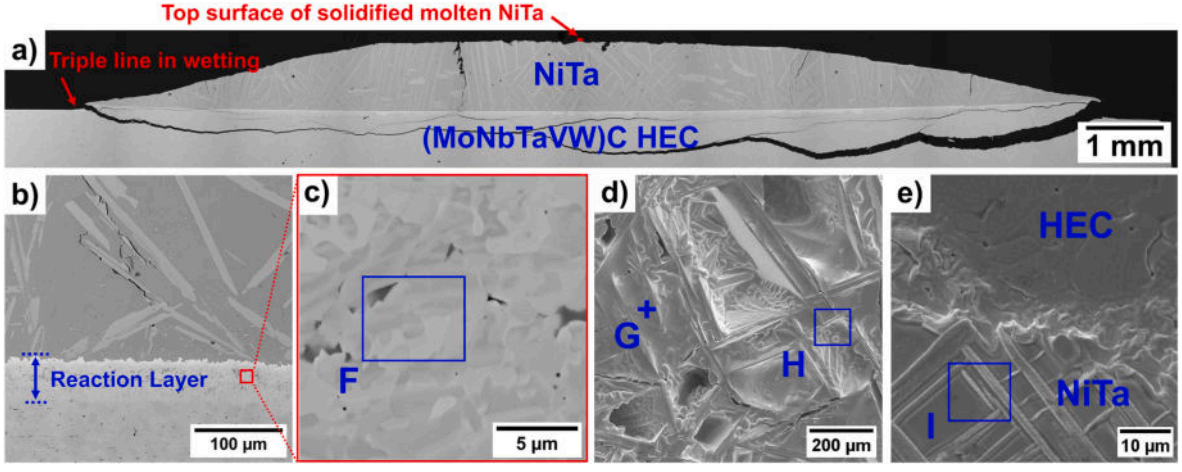


**Fig. 7.** a-c) SEM microstructure of the cross-section of HEC/NiTa couple at different magnifications; d) SEM image of the top surface of solidified NiTa, and e) SEM image of a triple line in wetting highlighted in a) after the wetting experiment at 1480 °C.

**Table 1**
EDS results (at.%) recorded at different places, as shown in Figs. 5 and 7. (Carbon is excluded from the measurements).

| | Ni | Ta | Mo | Nb | V | W | Possible Phases |
|---|---|---|---|---|---|---|---|
| A | 92.6 | 0.9 | 1.9 | – | 1.2 | 3.4 | Ni (s,s) |
| B | 5.2 | 35.8 | 8.2 | 28.3 | 14.6 | 7.9 | $(Ta, Nb, V)_xC_y$ |
| C | 96.1 | – | 1.3 | – | 1.4 | 1.2 | Ni (s,s) |
| D | 2.8 | 34.1 | 8.5 | 31.2 | 15.6 | 7.8 | $(Ta, Nb, V)_xC_y$ |
| E | 72.7 | 8.1 | 3.8 | 6.8 | 4.9 | 3.7 | Ni (s,s) |
| F | 18.2 | 31.5 | 10.3 | 15.1 | 11.4 | 13.5 | – |
| G | 93.2 | 6.8 | – | – | – | – | $Ni_xTa_y$ (s, s) |
| H | 90.9 | 9.1 | – | – | – | – | $Ni_xTa_y$ (s, s) |
| I | 93.1 | 6.9 | – | – | – | – | $Ni_xTa_y$ (s, s) |

further confirmed through elemental distribution analysis, as demonstrated by the EDS mapping in Fig. 6. The molten Ni dissolved a significant amount of W, Mo, V, Ta, Nb, and C; however, ribbon-like areas containing undissolved Nb, Mo, and V were observed. The persistence of these elements in their solid form suggested their slower dissolution in molten Ni compared to other elements. The black flakes observed in the upper region of the SEM image (Fig. 6), which correspond to the areas of high carbon concentration, were attributed to graphite resulting from the Ni/HEC interaction. This observation is consistent with thermodynamic evaluations using ternary phase diagrams (shown above), which predicted that graphite would form as an equilibrium phase alongside saturated Ni liquid and carbide phases.

The wetting study of molten Ni on the HEC surface experimentally validated the theoretical predictions, concluding that molten Ni substantially dissolves carbides. To mitigate this issue, CALPHAD calculations identified Ta as the most suitable alloying element for Ni. Subsequently, the wetting behaviour of NiTa alloy on the HEC surface was further studied.

### 3.4. Wetting of HEC by molten NiTa alloy

The NiTa alloy exhibited similar wetting kinetics to that of pure Ni on the HEC surface (Fig. 4a and 4c). During the initial stage of alloy spreading (Stage I), the molten NiTa alloy reached a contact angle of $\leq 15^{\circ}$, which stabilised in the second stage (Stage II). Such a low contact angle indicates a strong affinity and interaction between the NiTa alloy and the HEC substrate, promoting the formation of a robust interfacial bond.

Similar to Ni wetting, cross-sectional SEM analysis (Fig. 7) revealed the presence of cracks due to the thermal residual stresses that developed upon rapid cooling from the wetting temperature, as discussed earlier. In contrast to the concave dissolution profile observed for Ni wetting, the NiTa alloy exhibited a horizontal interface with the HEC ceramic, confirming a significant suppression of dissolution (Fig. 7a). This was clearly confirmed by the SEM/EDS analysis of the top surface of solidified NiTa alloy (Fig. 7d and e), as no significant content of elements originating from the HEC substrate was observed (Table 1).

A reaction layer with a thickness of ~50 μm formed at the interface (Fig. 7b). The interfacial region, depicted in Fig. 7c, exhibited a lower amount of Ni (18.2 at.%, Table 1) compared to the corresponding area observed in Ni wetting (Fig. 5c). The EDS mapping of the interaction layer of the NiTa/HEC couple (Fig. 8) revealed interdiffusion beyond the HEC ceramic surface, indicating significant reactions between the materials. Notably, the EDS maps confirmed the limited dissolution of the HEC ceramic into the NiTa alloy, which contradicts the behaviour observed for pure Ni (Fig. 6). This suggests a more controlled interfacial interaction, likely attributed to the specific composition of the NiTa alloy. The presence of Ta in the molten alloy facilitated the formation of Ta-rich phases (likely carbides) at the interface (Fig. 8). This almost continuous interfacial layer acted as a diffusion barrier, reducing excessive dissolution and enhancing interfacial stability. These findings demonstrate the potential of NiTa alloy as a promising brazing filler for (MoNbTaVW)C ceramics.

### 3.5. Brazing of HEC using the NiTa filler

The SEM microstructure of the cross-sectioned HEC/$Ni_{82.7}Ta_{17.2}$/HEC sample is presented in Fig. 9. A dense and uniform interfacial layer was observed at the metal-ceramic interface, indicating strong bonding. The resulting interfacial layer was symmetric and free of voids or microcracks. In contrast to the rapid cooling used in sessile-drop wetting experiments, which induced cracking due to CTE mismatch between HEC (~$7.65 \times 10^{-6}$ $K^{-1}$) and Ni (15.4 – 19 × $10^{-6}$ $K^{-1}$) [48,49], the brazing process in this work employed a controlled slow cooling rate of ~15 °C/min from the brazing temperature to room temperature. It is well known that avoiding thermal shock through gradual cooling is crucial to suppress the crack formation during the brazing of ceramics with a metallic filler [51,52]. Under these conditions, most of the residual stresses arising from CTE differences are relaxed in the ductile braze filler, and no cracks were observed in the brazed joint microstructure (Fig. 9). Notably, the reaction layer exhibited a microstructure similar to that observed in NiTa alloy after the wetting experiment, but the layer was thicker (~80 μm) when compared to the one observed (~50 μm) after the wetting experiment. This can be attributed to the

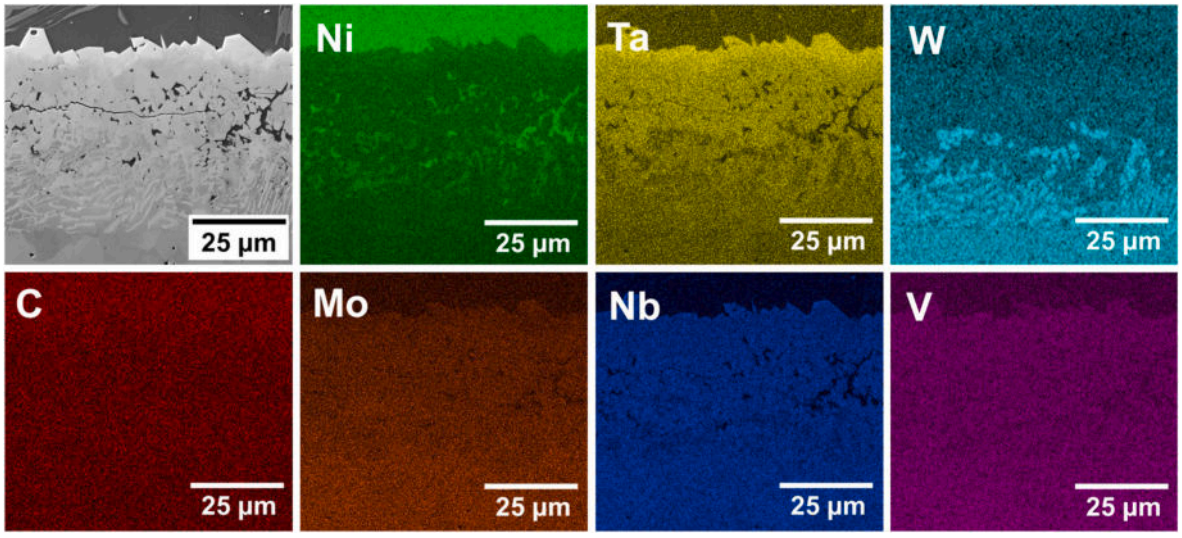


**Fig. 8.** SEM microstructure and corresponding EDS mapping of the cross-section of HEC/NiTa couple after the wetting experiment at 1480 °C.

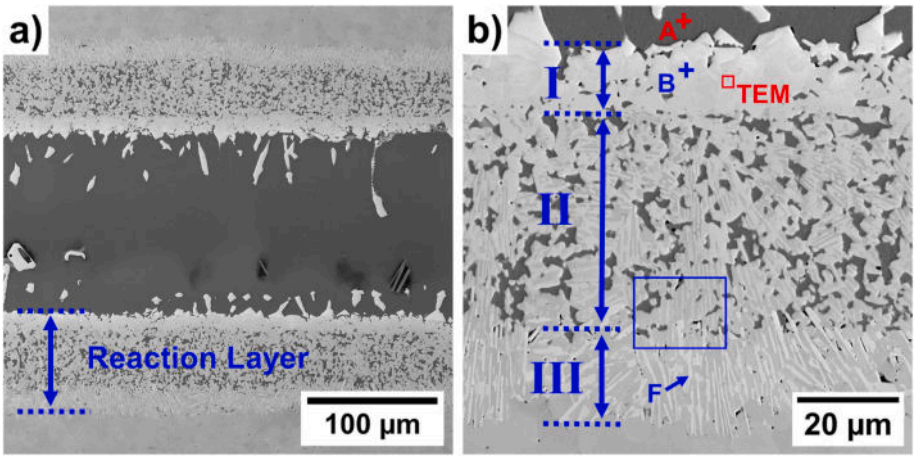


**Fig. 9.** SEM microstructure of the polished cross-section of HEC/NiTa/HEC joint brazed at 1480 °C for 5 min: a) overall view, b) reaction layer (blue square in Fig. 9a) at a higher magnification.

prolonged reaction time during the brazing. While in the wetting experiment, the HEC/NiTa couple was placed in the furnace after the temperature stabilised at 1480 °C and then rapidly extracted from the hot to the cold zone of the furnace, on the other hand, during the brazing process, the HEC/NiTa/HEC assembly underwent heating and cooling cycles in the FAST machine, with a heating rate of 100 °C/min and a cooling rate of 15 °C/min. These distinct thermal conditions significantly influenced the reaction kinetics, leading to the observed variation in layer thickness due to the extended duration of the brazing process.

Fig. 9b shows the NiTa/HEC interaction layer that can be divided into three distinct layers, while the EDS results of the selected points are given in Table 2. The analysis of the filler region adjacent to the reaction layer (labelled A) revealed a high concentration of Ni (84.7 at.%), with minor contributions from elements originating from the ceramics. The upper part of the reaction layer (layer I), in contact with NiTa, was approximately 15 μm thick and contained large, irregular grains similar to those distributed within the NiTa filler (Fig. 9a). This layer mainly consisted of Ta (68.1 at.%) carbide-rich phases, while small amounts of elements originating from the ceramics, such as Mo, W, Nb, and V (labelled B), and a minimal Ni content (1.3 at.%) were also detected (Table 2). This behaviour is consistent with the wetting experiments, where similar reactions between Ta and C led to the formation of Ta carbide-rich phases at the interface (Fig. 6).

To achieve a more detailed understanding of the interfacial structure and chemical interactions, TEM analysis was performed on selected regions of the metal–ceramic interface highlighted by "TEM" in Fig. 9b. The FIB technique was utilised to extract the sample from the aforementioned region. High-angle annular dark-field (HAADF) imaging and the corresponding EDS elemental maps (Fig. 10a) revealed distinct contrast between phases due to differences in atomic number, clearly outlining the interface and highlighting differences in phase morphology. Semiquantitative EDS analysis from three representative grains (points 1–3) is summarised in Table 3. The grains 1 and 2 showed a high concentration of Ta (≈69–71 at.%) along with minor amounts of Mo, Nb, V, W, and carbon in the range of 9.6–12.0 at.%, consistent with the composition of TaC. The selected area electron diffraction (SAED) patterns obtained from these grains (Fig. 10e and f) exhibit reflections indexed to the face-centred cubic (FCC) structure of TaC (PDF#35–0801), further confirmed by the high-resolution TEM (HRTEM) images (Fig. 10b and c), where the (111) lattice planes are clearly resolved. A slight difference in interplanar spacing was observed between the two grains: 0.2532 nm for grain 1 and 0.2586 nm for grain 2. This variation is likely related to the difference in chemical composition, particularly the higher Nb and lower carbon content in grain 2, which may influence the lattice parameter due to the substitutional incorporation of alloying elements into the TaC lattice [53,54]. On the other hand, grain 3, exhibited a markedly different composition, with 75.9 at.% Ni, 13.4 at.% Ta, and a reduced carbon content of 3.9 at.%. The corresponding SAED pattern (Fig. 10g) and HRTEM image (Fig. 10d) confirmed the presence of a metallic $Ni_8Ta$ phase (PDF#23–0438), characterised by the (301), (330), and (03 $\bar{1}$) reflections. These findings indicate the localised crystallisation of a Ni–Ta intermetallic compound within the minority dark grains in the reaction Layer I (Fig. 9b). In summary, the TEM analysis clearly confirmed the predominance of $TaC_x$ formation in Layer I, along with the presence of Ni-rich secondary phases.

Fig. 11 displays SEM microstructure and EDS mapping of the transition zone between layer II and layer III (highlighted by a rectangle in Fig. 9b), while the EDS results of the selected areas are given in Table 2. Layer II represents the region where molten Ni (79.7 at.%) infiltrated the ceramics (labelled C), reacting with the substrate and becoming entrapped within newly formed Ta–Nb-rich phases (labelled D), which also contained all the elements originating from the ceramics. Ta-rich (46.8 at.%) needle-like phases (labelled E) were observed within the grey Ta–Nb rich grains (labelled D), suggesting that a phase separation occurred. Such a bidirectional diffusion at the interface contributed to the thickening of the reaction layer, resulting in a 43 μm thick layer II.

The area furthest from the interface (layer III), exhibiting a thickness of ~21 μm, contained bright grey needle-like phases (labelled F), enriched in W (43.7 at.%) and Mo (33.9 at.%). Interestingly, almost the same amount of V (~14–15 at.%) was detected for all "D", "E", and "F" phases, suggesting that vanadium did not take part in the phase separation. Both needle-like phases (E and F) in layers II and III exhibited a columnar growth morphology, oriented perpendicular to the joining interface. This phase separation agrees well with the wetting results of pure Ni on the HEC substrate, where W, Mo, and V remained unsolved when in contact with molten Ni.

**Table 2**
EDS results (at.%) recorded at different places, as shown in Figs. 9b and 11. (Carbon is excluded from the measurements).

| | Ni | Ta | Mo | Nb | V | W | Possible phases |
|---|---|---|---|---|---|---|---|
| A | 84.7 | 3.1 | 3.6 | 0.2 | 2.5 | 5.9 | $Ni_xTa_y$ (s,s) |
| B | 1.3 | 68.1 | 5.5 | 11.9 | 8.7 | 4.5 | $TaC_x$ |
| C | 79.7 | 3.2 | 4.4 | 1.3 | 3.2 | 8.2 | $Ni_xTa_y$ (s,s) |
| D | 1.2 | 38.1 | 11.2 | 23.4 | 15.8 | 10.3 | $(Ta, Nb, V)_xC_y$ |
| E | 1.3 | 46.8 | 10.3 | 18.9 | 14.1 | 8.6 | $(Ta, Nb, V)_xC_y$ |
| F | 1.4 | 6.4 | 33.9 | – | 14.6 | 43.7 | $(W, Mo, V)_xC_y$ |

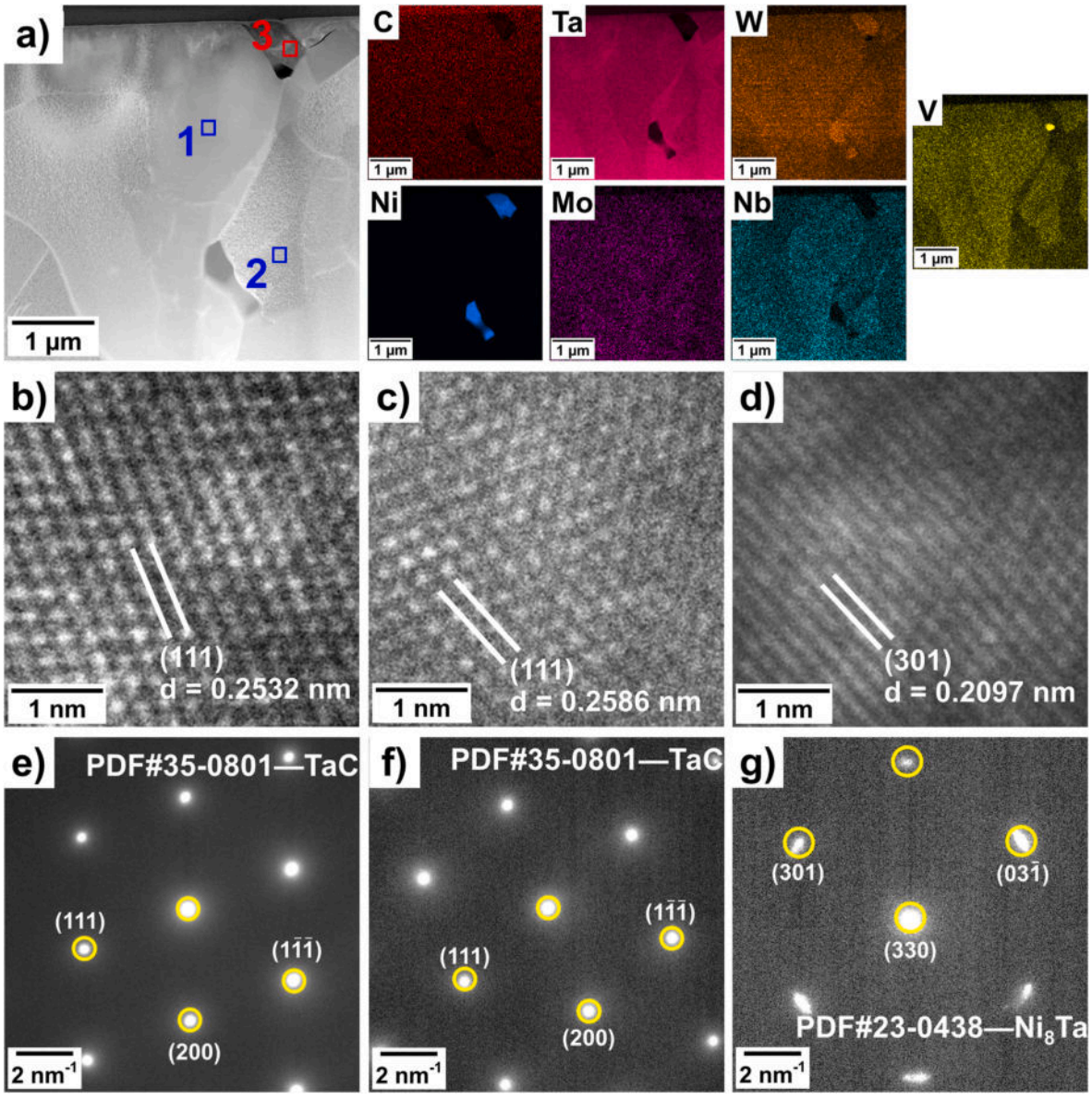


**Fig. 10.** HAADF-TEM image of layer I with corresponding elemental EDS maps (a); HRTEM images from regions 1, 2, and 3 are shown in (b), (c), and (d), respectively; Selected area electron diffraction (SAED) patterns acquired from the same regions are presented in (e–g), respectively.

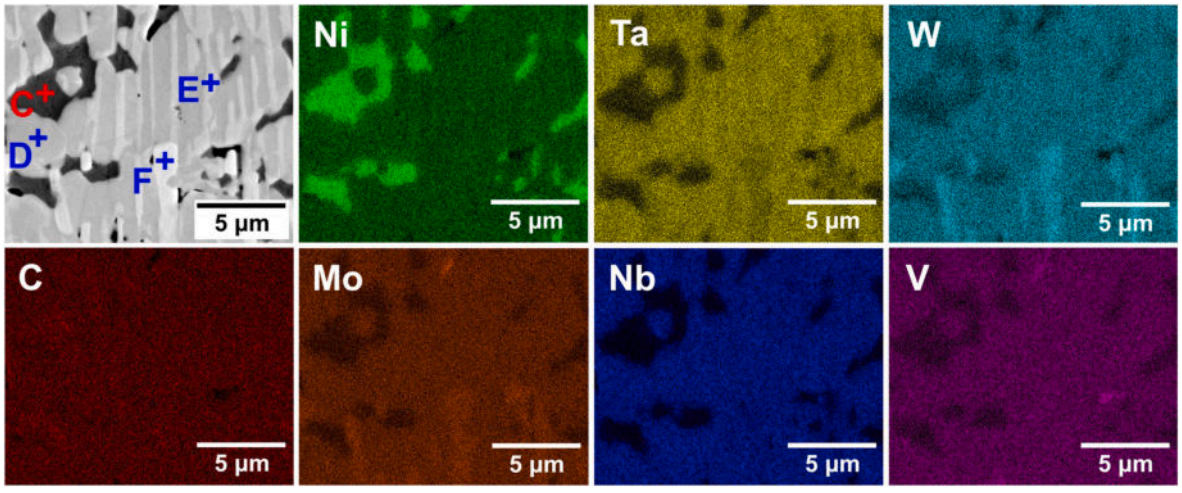


**Fig. 11.** Detailed SEM microstructure of the selected area in the reaction layer (blue rectangle in Fig. 9b) and corresponding EDS mapping.

**Table 3**
Semiquantitative EDS results from areas 1–3, as shown in Fig. 10a.

| | Ni | Ta | Mo | Nb | V | W | C | Phases |
|---|---|---|---|---|---|---|---|---|
| 1 | 0 | 69.1 | 3.1 | 8.9 | 6.1 | 0.7 | 12.1 | TaC |
| 2 | 0 | 71.1 | 2.8 | 10.6 | 5.6 | 0.3 | 9.6 | TaC |
| 3 | 75.9 | 13.4 | 1.9 | 0.7 | 2.3 | 1.9 | 3.9 | $Ni_8Ta$ |

### 3.6. Brazing mechanism

The brazing mechanism of (MoNbTaVW)C HEC ceramics using the NiTa filler (illustrated in Fig. 12) can be understood through phase analysis related to Figs. 9–11. Initially, below the melting point of the filler, Ni diffuses into the rock-salt structure of HEC, substituting transition metal cations, such as Ta, Nb, Mo, V, and W due to similar atomic radii and valency (Fig. 12a) [26].

Upon melting of the NiTa alloy, the high chemical reactivity of Ni leads to an extensive dissolution of HEC constituents (Fig. 12b). Due to the high formation energy and weaker Ni–C bonding [55], Ni preferentially segregates as a Ni-rich solid solution, dissolving the metallic elements from HEC, similarly to what was observed in pure Ni wetting (Fig. 5). This carbide dissolution in Ni-based alloys has been observed previously [26,29,56].

As brazing progresses (Fig. 12c), Ni continues to dissolve elements from HEC, leading to the formation of an interfacial reaction layer. Simultaneously, Ta from the filler reacts with liberated carbon from the ceramics to form a nearly continuous $TaC_x$-rich layer. This layer acts as a diffusion barrier, limiting further Ni infiltration and HEC dissolution. In the NiTa/HEC system, the formation of the $TaC_x$ layer establishes thermodynamic equilibrium, stabilising the joint and preventing further dissolution. However, in the Ni/HEC system, dissolution continues without interruption, resulting in degradation of the ceramics. The formation of such a continuous $TaC_x$ layer has been reported in other NiTa brazing studies [36].

As the $TaC_x$-rich layer thickens, residual Ni trapped within layer II may continue to interact with the ceramic phases. Due to differences in solubility and chemical potential, phase separation likely occurs within the ceramic constituents, leading to selective dissolution and redistribution of elements. It is plausible that phases enriched in Ta and Nb tend to dissolve more readily into the Ni, while Mo–W-rich phases remain comparatively stable, manifesting as needle-like structures within the HEC ceramics (labelled F). The limited solubility of transition metals in Ni, combined with ongoing reactions involving Ta and C at the interface, could drive a compositional gradient that promotes the phase separation of Ta- and Nb-containing species towards the growing $TaC_x$-rich layer. This process may involve diffusion through existing channels and incorporation into the $TaC_x$ phase, contributing to the formation of needle-like precipitates. Such phase separation and redistribution phenomena could enhance joint stability by impeding further dissolution and reinforcing interfacial integrity.

### 3.7. Mechanical properties of HEC brazed with NiTa

The nanoindentation was employed to determine the hardness and indentation elastic modulus across the joining area in the HEC/NiTa/HEC joints (Fig. 13). The position "0" represents the area approximately in the middle of the NiTa interlayer, while the other positions indicate their respective distances from this centre. Generally, the hardness and indentation elastic modulus of the ceramics and reaction regions exhibited higher values compared to the interlayer, displaying a similar overall trend. In the ceramic region, the hardness and indentation elastic modulus increased from 22 GPa to 310 GPa at the position of −275 μm to their higher values of 27 and 328 GPa at −185 μm, respectively. In other words, the hardness and indentation elastic modulus of the HEC substrate increased in a direction towards the interface. This can likely be attributed to the residual stresses induced by the mismatch in the coefficients of thermal expansion (CTE) between HEC ceramics and NiTa alloy. The CTE of HEC ceramics measured in this work was ~$7.65 \times 10^{-6}\ K^{-1}$, while the CTE of Ni-based superalloy ranges from $15.4 - 19 \times 10^{-6}\ K^{-1}$ [48,49]. Mishra et al. demonstrated that a lower CTE of ceramic components induces compressive stresses within the ceramics during brazing and subsequent interactions with metals [21]. These compressive stresses have been shown to contribute to an increase in hardness and indentation elastic modulus in this specific ceramic region [57]. Since the CTE of NiTa is approximately double that of HEC

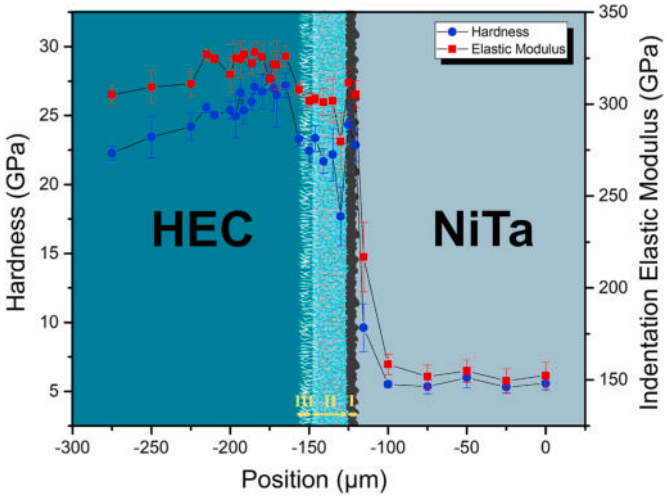


**Fig. 13.** Hardness and indentation elastic modulus of HEC/NiTa/HEC joint measured by nanoindentation at the load of 250 mN.

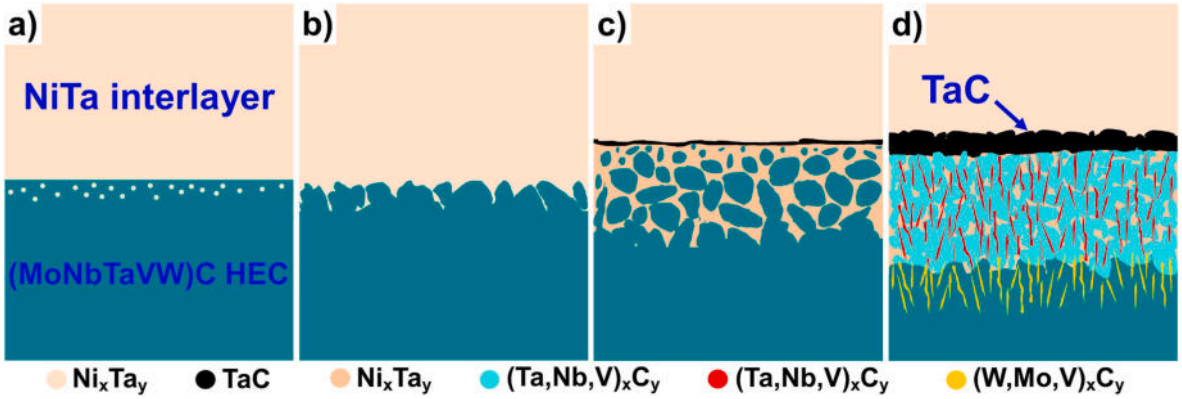


**Fig. 12.** Schematic illustration of the brazing mechanism of HEC ceramics using NiTa at 1480 °C.

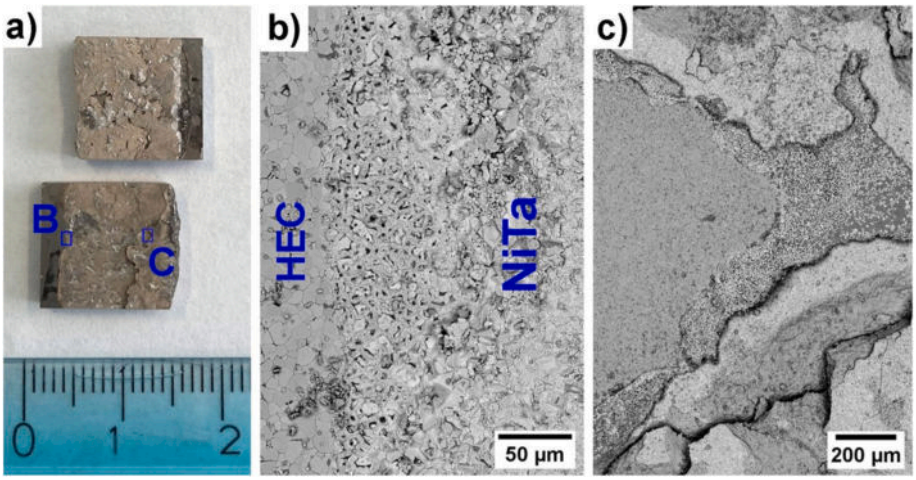


**Fig. 14.** a) Macro image of the fracture surfaces of NiTa-brazed HEC after single lap offset shear strength test; b) and c) SEM microstructures of the selected area in Fig. 14a.

ceramics, significant residual stresses are expected to develop within the ceramic part. This likely explains the increase in hardness and indentation elastic modulus of the HEC near the interface, as observed in the present work.

Within the reaction layer, at positions −150 μm and −155 μm (corresponding to layer III in Fig. 9b), the hardness and indentation elastic modulus were 23 and 305 GPa, respectively. These values were lower than those observed in the ceramic area adjacent to the reaction layer. At the position of −130 μm (representing layer II in Fig. 9b), the lowest hardness and indentation elastic modulus within the reaction layer were observed (17.7 and 280 GPa, respectively), which can be attributed to the presence of nickel from the brazing alloy in the ceramic area close to the interface. On the contrary, the highest hardness and indentation elastic modulus (24 GPa and 311 GPa, respectively) were observed in the region between −120 μm and −125 μm (corresponding to layer I in Fig. 9b), due to the formation of a continuous $TaC_x$-rich layer (see Fig. 9).

The NiTa interlayer exhibited relatively constant hardness and indentation elastic modulus (5.3 and 150 GPa, respectively). This region, characterised by a high Ni content (approximately 84.7 at.%, as shown in Table 2), exhibited lower hardness and indentation elastic modulus compared to the reaction layer and the ceramic regions. In summary, the observed variations in mechanical properties across the reaction zone and adjacent areas highlight the critical influence of compositional gradients, interfacial phase formation, and residual stresses on the overall mechanical performance of NiTa brazed HEC ceramics.

The strength of the brazed HEC ceramics was evaluated using a single-lap offset shear test (detailed test condition described in section 2.5) at room temperature, resulting in a high average shear strength of 220 ± 17 MPa. This value exceeds those reported for active brazing of similar ceramics. For example, (MoNbTaVW)C brazed with a Ti–Zr–Ni–Cu filler alloy exhibited a shear strength of 193 MPa [32], while (HfTaZrNbTi)C brazed with a TiNi–20Nb eutectic alloy showed a lower strength of 167 MPa [27]. The relatively high strength achieved in this study for the (MoNbTaVW)C joints brazed with NiTa alloy can be attributed to several factors, including the crack-hole-free interfacial interactions, the formation of stable intermediate phases through chemical reactions, and the favourable microstructure of the reaction area.

Microstructural analysis revealed that the interfacial phases contained elements from both the HEC ceramics and the NiTa filler, demonstrating good material compatibility. Furthermore, considering the bonding region as a composite system, the perpendicular needle-like phases observed in layers II and III (labelled E and F in Fig. 11) act as crucial structural reinforcements within the matrix. This significantly contributes to the increase in strength. It was reported that in composite systems, reinforcement phases oriented perpendicularly to the applied stress direction play a crucial role in enhancing the mechanical properties of the bond [58]. This orientation enables efficient load transfer at the reinforcement-matrix interface, minimising deformation and increasing strength [59]. In addition, these needle-like phases enhance mechanical interlocking and facilitate more effective stress distribution within the joint [60]. Consequently, the exceptional strength and reliability of the brazed joint in the present work can be attributed to the synergic effects of chemical compatibility, optimised stress distribution, and robust mechanical interlocking facilitated by the presence of these needle-like reinforcement phases within the interaction layer.

Fig. 14 illustrates the macro image (Fig. 14a) and SEM images (Figs. 14b and c of the selected areas) of the fracture surface of the NiTa-brazed HEC ceramics. The failure predominantly occurred within the interlayer, as evidenced by the presence of interlayer on both fracture surfaces (Fig. 14a). This observation indicates a cohesive fracture mechanism, where the crack propagated through the interlayer rather than along the ceramic parts or the metal/ceramics interface. Such behaviour strongly suggests a high-strength bond between the NiTa interlayer and the HEC ceramic, effectively preventing the crack from propagating into the ceramic substrate [61,62]. The cohesive nature of the fracture underscores the robust adhesion achieved during the brazing process, as reflected by the high shear strength of 220 ± 17 MPa. This result highlights the effectiveness of NiTa alloy in creating a strong and durable bond with HEC ceramics, suggesting its potential for reliable joining applications.

## 4. Conclusions

This study investigated the wetting and interfacial reactions between pure Ni and a NiTa alloy in contact with (MoNbTaVW)C high entropy carbide ceramics. Utilising CALPHAD calculations of ternary phase diagrams, wetting experiments by the sessile-drop technique, and brazing via the FAST technique at 1480 °C, the following key findings were observed.

- Pure Ni exhibited significant reactivity with the HEC surface, resulting in extensive ceramic dissolution and a low wetting angle (≤15°).
- The addition of 17.2 at.% Ta to Ni significantly reduced interfacial reactions and dissolution of HEC, while maintaining excellent wetting behaviour with the final wetting angle of ≤15°. Furthermore, the incorporation of Ta into the filler led to the formation of a $TaC_x$

layer along the interface, which effectively acted as a barrier to dissolution.

- The hardness and indentation elastic modulus measurement of the phases in the interaction layer by nanoindentation investigation confirmed that the $TaC_x$ phases have relatively high values of 24 GPa and 311 GPa, respectively.
- Successful joining of HEC ceramics was achieved using a NiTa interlayer, resulting in a high shear strength of 220 ± 17 MPa. This high strength was attributed to the combination of chemical compatibility at the interface, favourable thermal matching of the formed phases, and the beneficial influence of needle-like reinforcing phases within the microstructure of the interface.

## Credit authorship contribution statement

Naser Hosseini – conceptualization; data curation; investigation; visualization; writing – original draft, Fabrizio Valenza – conceptualization; methodology; validation; visualization; writing – review & editing, Zdeněk Chlup – methodology; validation, Sofia Gambaro – investigation; data curation; writing – review & editing, Filip Šiška – investigation, Carla Malinverni – investigation, Jie Xu – investigation, Valentina Casalegno – methodology; investigation, Alexandra Kovalčíková; – investigation, Monika Tatarková; – investigation; data curation, Milena Salvo – investigation; validation, Xiaobing Zhou – investigation; validation; funding acquisition, Ivo Dlouhý; – validation; funding acquisition; formal analysis, Peter Tatarko – conceptualization; supervision; validation; visualization; funding acquisition; writing – review & editing.

## Declaration of competing interest

The authors declare that they have no known competing financial interests or personal relationships that could have appeared to influence the work reported in this paper.

## Acknowledgment

This work was supported by the Slovak Research and Development Agency under the Contract no. SK-CZ-RD-21-0089, APVV-21-0402, and APVV-SK–CN–23-0015. The support of projects LUASK22219 and SAS-TUBITAK/JRP/2023/807/HiTemCom (No. 720464) is also acknowledged. The authors are grateful to the JECS Trust for funding [the visit of Naser Hosseini to ICMATE-CNR in Genoa.] (Contract No. 2022334). The authors also express their gratitude to Prof. Gabriele Cacciamani of the University of Genoa for granting permission to use the GHEA database in the thermodynamic calculations. X.Z. acknowledges the support from the Ningbo Youth Science and Technology Innovation Leading Talent Project (2023QL043) and International Exchange Projects of the 9th Meeting of the China Slovakia Science and Technology Cooperation Committee (No. 9–6).

## References

[1] Fang Y, Zhao S, Li C, Wu Y, Li J, Fan H. Mechanical and tribological performance of (TiNbTaWMo)C high-entropy ceramics in a wide temperature range. J Mater Res Technol 2023;24:6312–21. https://doi.org/10.1016/j.jmrt.2023.04.220.

[2] Wang Z, Li Z-T, Zhao S-J, Wu Z-G. High-entropy carbide ceramics: a perspective review. Tungsten 2021;3:131–42. https://doi.org/10.1007/s42864-021-00085-7.

[3] Dusza J, Csanádi T, Medveď D, Sedlák R, Vojtko M, Ivor M, et al. Nanoindentation and tribology of a (Hf-Ta-Zr-Nb-Ti)C high-entropy carbide. J Eur Ceram Soc 2021;41:5417–26. https://doi.org/10.1016/j.jeurceramsoc.2021.05.002.

[4] Li C, Gao R, Ouyang H, Shen T, Chen Z, Li Y. Hierarchical porous ($Ta_{0.2}$ $Nb_{0.2}$ $Ti_{0.2}$ $Zr_{0.2}$ $Hf_{0.2}$)C high-entropy ceramics prepared by a self-foaming method for thermal insulation. J Adv Ceram 2024;13:956–66. https://doi.org/10.26599/JAC.2024.9220909.

[5] Xu H, Jiang L, Chen K, Huang Q, Zhou X. High-entropy rare-earth diborodicarbide: a novel class of high-entropy ($Y_{0.25}$ $Yb_{0.25}$ $Dy_{0.25}$ $Er_{0.25}$)$B_2$ $C_2$ ceramics. J Adv Ceram 2023;12:1430–40. https://doi.org/10.26599/JAC.2023.9220765.

[6] Zhang J, Liang J, Li H, Yang Y, Huo D, Liu C. A review of high-entropy ceramics preparation methods, properties in different application fields and their regulation methods. J Mater Res Technol 2024;32:1083–117. https://doi.org/10.1016/j.jmrt.2024.07.153.

[7] Castle E, Csanádi T, Grasso S, Dusza J, Reece M. Processing and properties of high-entropy ultra-high temperature carbides. Sci Rep 2018;8:8609. https://doi.org/10.1038/s41598-018-26827-1.

[8] Wei X-F, Liu J-X, Li F, Qin Y, Liang Y-C, Zhang G-J. High entropy carbide ceramics from different starting materials. J Eur Ceram Soc 2019;39:2989–94. https://doi.org/10.1016/j.jeurceramsoc.2019.04.006.

[9] Pötschke J, Dahal M, Herrmann M, Vornberger A, Matthey B, Michaelis A. Preparation of high-entropy carbides by different sintering techniques. J Mater Sci 2021;56:11237–47. https://doi.org/10.1007/s10853-021-06004-y.

[10] Medveď D, Ivor M, Kovalčíková A, Múdra E, Csanádi T, Sedlák R, et al. Wear behavior of (Mo–Nb–Ta–V–W)C high-entropy carbide. Int J Appl Ceram Technol 2023;20:224–35. https://doi.org/10.1111/ijac.14111.

[11] Li Z, Wang Z, Wu Z, Xu B, Zhao S, Zhang W, et al. Phase, microstructure and related mechanical properties of a series of (NbTaZr)C-Based high entropy ceramics. Ceram Int 2021;47:14341–7. https://doi.org/10.1016/j.ceramint.2021.02.013.

[12] Liu G, Zhang X, Yang J, Qiao G. Recent advances in joining of SiC-based materials (monolithic SiC and SiCf/SiC composites): joining processes, joint strength, and interfacial behavior. J Adv Ceram 2019;8:19–38. https://doi.org/10.1007/s40145-018-0297-x.

[13] Zhou X, Shi L, Zou S, Xu J, Liu Y, Tatarko P. Fast seamless joining of $SiC_w$/$Ti_3SiC_2$ composite using electric field-assisted sintering technique. Int J Appl Ceram Technol 2021;18:1670–6. https://doi.org/10.1111/ijac.13799.

[14] Huang C-C, Chen J, Zhu M, Li F-F, Huang Z-R. Joining of SiC ceramics using high-silicon aluminum alloy fillers assisted by laser cladding. J Mater Res Technol 2023;24:5675–86. https://doi.org/10.1016/j.jmrt.2023.04.215.

[15] Jiang N, Song X, Bian H, Song X, Wang M, Long W, et al. Interfacial microstructure evolution and mechanical properties of Al2O3/Al2O3 joints brazed with Ti–Ni–Nb filler metal. J Mater Res Technol 2023;24:3901–12. https://doi.org/10.1016/j.jmrt.2023.04.088.

[16] Yang H, Zhou X, Shi W, Wang J, Li P, Chen F, et al. Thickness-dependent phase evolution and bonding strength of SiC ceramics joints with active Ti interlayer. J Eur Ceram Soc 2017;37:1233–41. https://doi.org/10.1016/j.jeurceramsoc.2016.12.009.

[17] Malinverni C, Salvo M, Ziętara M, Cempura G, Kruk A, Maier J, et al. A yttrium aluminosilicate glass-ceramic to join SiC/SiC composites. J Eur Ceram Soc 2024;44:3579–87. https://doi.org/10.1016/j.jeurceramsoc.2023.12.095.

[18] Grasso S, Tatarko P, Rizzo S, Porwal H, Hu C, Katoh Y, et al. Joining of β-SiC by spark plasma sintering. J Eur Ceram Soc 2014;34:1681–6. https://doi.org/10.1016/j.jeurceramsoc.2013.12.023.

[19] Gambaro S, Valenza F, Passerone A, Cacciamani G, Muolo ML. Brazing transparent YAG to Ti6Al4V: reactivity and characterization. J Eur Ceram Soc 2016;36:4185–96. https://doi.org/10.1016/j.jeurceramsoc.2016.05.022.

[20] Zhao W, Zhang S, Yang J, Lin T, Sekulic DP, He P. Wetting and brazing of YIG ceramics using Ag–CuO–TiO2 metal filler. J Mater Res Technol 2021;10:1158–68. https://doi.org/10.1016/j.jmrt.2020.12.080.

[21] Mishra S, Sharma A, Jung DH, Jung JP. Recent advances in active metal brazing of ceramics and process. Met Mater Int 2020;26:1087–98. https://doi.org/10.1007/s12540-019-00536-4.

[22] Wang G, Liu Y, Wang M, Yang Y, Zhao Y, He R, et al. Brazing of Ti-coated SiC using a CoFeCrNiCu high entropy alloy filler via electric field-assisted sintering. J Mater Res Technol 2023;23:5142–51. https://doi.org/10.1016/j.jmrt.2023.02.134.

[23] Sun KB, Yang ZW, Mu RJ, Niu SY, Wang Y. Active brazing of (HfTaZrNbTi)C high-entropy carbide ceramic and Nb with Ti Ni composite interlayer: novel findings on the reaction layer. Mater Char 2023;203:113103. https://doi.org/10.1016/j.matchar.2023.113103.

[24] Pötschke J, Vornberger A, Gestrich T, Berger L-M, Michaelis A. Influence of different binder metals in high entropy carbide based hardmetals. Powder Metall 2022;65:373–81. https://doi.org/10.1080/00325899.2022.2076311.

[25] Anwer Z, Cabezas L, Jiménez-Piqué E, Llanes L, Vleugels J, Huang S. Facile synthesis of high entropy carbide-nickel based cermets by in-situ carbo-thermal reduction of transition metal oxides. Acta Mater 2024;272:119924. https://doi.org/10.1016/j.actamat.2024.119924.

[26] Mu RJ, Yang ZW, Niu SY, Sun KB, Wang Y, Wang DP. Diffusion bonding of (Hf0.2Zr0.2Ti0.2Ta0.2Nb0.2)C high-entropy ceramic with metallic Ni foil. J Eur Ceram Soc 2021;41:7478–87. https://doi.org/10.1016/j.jeurceramsoc.2021.08.048.

[27] Sun K, Yang Z, Mu R, Niu S, Wang Y, Wang D. Densification and joining of a (HfTaZrNbTi)C high-entropy ceramic by hot pressing. J Eur Ceram Soc 2021;41:3196–206. https://doi.org/10.1016/j.jeurceramsoc.2020.12.043.

[28] Wang P, Xu Z, Qin B, Lin J, Cao J, Feng J, et al. Active brazing of high entropy ceramic and Nb metal: interfacial microstructure and brazing mechanism. Vacuum 2022;205:111464. https://doi.org/10.1016/j.vacuum.2022.111464.

[29] Vedel D, Storozhenko M, Mazur P, Konoval V, Skoryk M, Grigoriev O, et al. Wetting and interfacial behavior of Fe, Co, Ni on (Ti, Zr, Hf, Nb, Ta)C high entropy ceramics. Open Ceramics 2023;15:100393. https://doi.org/10.1016/j.oceram.2023.100393.

[30] Mu R, Wang Y, Niu S, Sun K, Yang Z. Wetting of FeCoCrNiTi0.2 high entropy alloy on the (HfZrTiTaNb)C high entropy ceramic. J Eur Ceram Soc 2023;43:7263–72. https://doi.org/10.1016/j.jeurceramsoc.2023.07.065.

[31] Mu R, Wang Y, Niu S, Sun K, Yang Z. Enhanced interfacial structure of (HfZrTiTaNb)C high-entropy ceramic joint brazed using FeCoCrNiTi0.2 alloy filler. J Mater Process Technol 2024;324:118253. https://doi.org/10.1016/j.jmatprotec.2023.118253.

[32] Niu S, Yang Z, Mu R, Sun K, Wang Y. Varying interfacial reaction patterns in (VNbTaMoW)C ceramic joints brazed with Ti-Zr-Ni-Cu filler alloy. J Eur Ceram Soc 2024. https://doi.org/10.1016/j.jeurceramsoc.2024.03.023.
[33] Xu J, Zhou X, Huang Q. Joule heating enables ultra-fast SiC ceramics joining in seconds. Scr Mater 2025;264:116721. https://doi.org/10.1016/j.scriptamat.2025.116721.
[34] Hosseini N, Valenza F, Chlup Z, Gambaro S, Malinverni C, Casalegno V, et al. Wetting and brazing of (HfTaZrNbTi)B2 and (HfTaZrNbTi)C high-entropy ceramics by AgCuTi filler. Open Ceramics 2025;22:100792. https://doi.org/10.1016/j.oceram.2025.100792.
[35] Passerone A, Muolo ML, Valenza F, Monteverde F, Sobczak N. Wetting and interfacial phenomena in Ni–HfB2 systems. Acta Mater 2009;57:356–64. https://doi.org/10.1016/j.actamat.2008.09.016.
[36] Valenza F, Gambaro S, Muolo ML, Cacciamani G, Tatarko P, Saunders TG, et al. Wetting and interfacial phenomena of Ni-Ta alloys on CVD-SiC. Int J Appl Ceram Technol 2017;14:295–304. https://doi.org/10.1111/ijac.12632.
[37] Valenza F, Muolo ML, Passerone A. Wetting and interactions of Ni- and Co-based superalloys with different ceramic materials. J Mater Sci 2010;45:2071–9. https://doi.org/10.1007/s10853-009-3801-4.
[38] Tillmann W, Bültena J, Wojarski L, Zajaczkowski J, Donnerbauer K, Walther F. Wetting behaviour of nickel-based brazing alloy BNi-5a on conventionally cast and laser-melted austenitic stainless steel 316L. J Mater Res Technol 2024;33:6701–13. https://doi.org/10.1016/j.jmrt.2024.10.228.
[39] Valenza F, Gambaro S, Muolo ML, Salvo M, Casalegno V. Wetting of SiC by Al-Ti alloys and joining by in-situ formation of interfacial Ti3Si(Al)C2. J Eur Ceram Soc 2018;38:3727–34. https://doi.org/10.1016/j.jeurceramsoc.2018.04.025.
[40] Okamoto H. Ni-Ta (Nickel-Tantalum). J Phase Equil 2000;21. https://doi.org/10.1361/105497100770339798. 497–497.
[41] Akram MY, Ferraris M, Casalegno V, Salvo M, Puchas G, Knohl S, et al. Joining and testing of alumina fibre reinforced YAG-ZrO2 matrix composites. J Eur Ceram Soc 2018;38:1802–11. https://doi.org/10.1016/j.jeurceramsoc.2017.11.026.
[42] Gambaro S, Fenocchio L, Valenza F, Riani P, Cacciamani G. Combined experimental and CALPHAD investigation of equimolar AlCoCrFeNiX (X=Mo,Ta, W) high-entropy alloys. Calphad 2024;85:102702. https://doi.org/10.1016/j.calphad.2024.102702.
[43] Gambaro S, Valenza F, Fenocchio L, Cacciamani G. Liquid AlCoCrFeNi and AlCoCrFeNiX (X = Mo, Ta) high-entropy alloys on graphite: wetting, reactivity and CALPHAD modelling. Surf Interfaces 2024;54:105207. https://doi.org/10.1016/j.surfin.2024.105207.
[44] Rado C, Kalogeropoulou S, Eustathopoulos N. Wetting and bonding of Ni–Si alloys on silicon carbide. Acta Mater 1999;47:461–73. https://doi.org/10.1016/S1359-6454(98)00374-7.
[45] Valenza F, Muolo ML, Passerone A, Cacciamani G, Artini C. Control of interfacial reactivity between ZrB2 and Ni-based brazing alloys. J Mater Eng Perform 2012;21:660–6. https://doi.org/10.1007/s11665-012-0127-1.
[46] Wheeler JM, Gan B, Spolenak R. Combinatorial investigation of the Ni–Ta system via correlated high-speed nanoindentation and EDX mapping. Small Methods 2022;6. https://doi.org/10.1002/smtd.202101084.
[47] Zhou C, Guo C, Li C, Du Z. Thermodynamic optimization of the Ni–Ta system supported by the key experiments. Thermochim Acta 2018;666:135–47. https://doi.org/10.1016/j.tca.2018.06.011.
[48] Hidnert P. Thermal expansion of some nickel alloys. J Res Natl Bur Stand 1957;58:89. https://doi.org/10.6028/jres.058.011. 1934.
[49] Sung PK, Poirier DR. Estimation of densities and coefficients of thermal expansion of solid Ni-base superalloys. Mater Sci Eng, A 1998;245:135–41. https://doi.org/10.1016/S0921-5093(97)00699-0.
[50] Deng Y, Liu R, Jiao K, Chen L, Chen Y. Evolution and mechanism of dissolutive wetting between hot metal and carbon brick. J Eur Ceram Soc 2022;42:4420–8. https://doi.org/10.1016/j.jeurceramsoc.2022.04.018.
[51] Zhang L. Filler metals, brazing processing and reliability for diamond tools brazing: a review. J Manuf Process 2021;66:651–68. https://doi.org/10.1016/j.jmapro.2021.04.015.
[52] Li C, Si X, Cao J, Qi J, Dong Z, Feng J. Residual stress distribution as a function of depth in graphite/copper brazing joints via X-ray diffraction. J Mater Sci Technol 2019;35:2470–6. https://doi.org/10.1016/j.jmst.2019.07.023.
[53] Lin D, Hu J, Wu R, Liu Y, Li X, SaGong MJ, et al. Multiscale plastic deformation in additively manufactured FeCoCrNiMo high-entropy alloys to achieve strength–ductility synergy at elevated temperatures. Int J Plast 2024;183:104142. https://doi.org/10.1016/j.ijplas.2024.104142.
[54] Cheng S, Hou T, Zhang D, Wang Z, Yin C, Pan X, et al. New insights into the formation mechanism of the multicomponent carbides (Nb, M)C (M = Ti, Cr and Mn). J Mater Res Technol 2024;28:1022–31. https://doi.org/10.1016/j.jmrt.2023.11.179.
[55] Khatri I, Szymanski NJ, Dumre BB, Amar JG, Gall D, Khare SV. Correlating structure and orbital occupation with the stability and mechanical properties of 3d transition metal carbides. J Alloys Compd 2022;891:161866. https://doi.org/10.1016/j.jallcom.2021.161866.
[56] Lin Q, Sui R. Wetting of carbide ceramics (B4C, SiC, TiC and ZrC) by molten Ni at 1753 K. J Alloys Compd 2015;649:505–14. https://doi.org/10.1016/j.jallcom.2015.07.138.
[57] Zhu Q, Zeng Y, Yang D, Zhu J, Zhuo L, Li J, et al. Measurement of the elastic modulus and residual stress of thermal barrier coatings using a digital image correlation technique. Coatings 2021;11:245. https://doi.org/10.3390/coatings11020245.
[58] Lassila LVJ, Tezvergil A, Dyer SR, Vallittu PK. The bond strength of particulate-filler composite to differently oriented fiber-reinforced composite substrate. J Prosthodont 2007;16:10–7. https://doi.org/10.1111/j.1532-849X.2006.00147.x.
[59] Jiang X, Gao Q. Stress-transfer analysis for fibre/matrix interfaces in short-fibre-reinforced composites. Compos Sci Technol 2001;61:1359–66. https://doi.org/10.1016/S0266-3538(01)00034-3.
[60] Kassam TA, Hari Babu N, Ludford N, Yan S, Howkins A. Secondary phase interaction at interfaces of high-strength brazed joints made using liquid phase sintered alumina ceramics and Ag-Cu-Ti braze alloys. Sci Rep 2018;8:3352. https://doi.org/10.1038/s41598-018-20674-w.
[61] Xin C, Yan J, Li N, Liu W, Du J, Cao Y, et al. Microstructural evolution during the brazing of Al 2 O 3 ceramic to kovar alloy by sputtering Ti/Mo films on the ceramic surface. Ceram Int 2016;42:12586–93. https://doi.org/10.1016/j.ceramint.2016.04.094.
[62] Gorjan L, Blugan G, Boretius M, La Pierre S De, Ferraris M, Casalegno V, et al. Fracture behavior of soldered Al2O3 ceramic to A356 aluminum alloy and resistance of the joint to low temperature exposure. Mater Des 2015;88:889–96. https://doi.org/10.1016/j.matdes.2015.09.067.